Research Article Vol. 30, No. 3 / 31 Jan 2022 / Optics Express 4515
Optics EXPRESS

Enhancement of Cryo-EM maps by a multiscale tubular filter

JAVIER VARGAS,[1,*] JOSÉ A. GÓMEZ-PEDRERO,[1] J. ANTONIO QUIROGA,[1,2] AND JOSÉ ALONSO[1,2]

[1]*Departmento de Óptica, Universidad Complutense de Madrid, 28040 Madrid, Spain*
[2]*Indizen Optical Technologies S.L., Parque Científico de Madrid, Faraday 7, 28049 Madrid, Spain*
[*]*jvargas@ucm.es*

Abstract: We present an approach to enhance cryo-electron microscopy (cryo-EM) postprocessed maps based on a multiscale tubular filter. The method determines a tubularness measure locally by the analysis of the eigenvalues of the Hessian matrix. This information is used to enhance elongated local structures and to attenuate blob-like and plate-like structures. The approach, thus, introduces *a priori* information in the reconstructions to improve their interpretability and analysis at high-resolution. The proposed method has been tested with simulated and real cryo-EM maps including recent reconstructions of the SARS-CoV-2. Our results show that our methods can improve obtained reconstructions.

1. Introduction

Cryo-electron microscopy (cryo-EM) is a mainstream technique for structure determination of macromolecular complexes at atomic resolution [1,2]. This approach can capture multiple conformations of the sample to infer their dynamics and function. Thus, cryo-EM allows the structural and functional understanding of macromolecules in their native conditions. This structural technique has shown to be essential in the global fight against the SARS-CoV-2. Wrapp et al., [3] and Walls et al., [4] obtained the first cryo-EM 3D reconstructions of the SARS-CoV-2 spike protein in the prefusion conformation. Since then, more than 808 cryo-EM reconstructions have been solved and analyzed for different SARS-CoV-2 related proteins, including mutational variants and complexes with antibodies (please see, https://www.emdataresource.org/coronavirus_search.html). This structural information is essential to produce more effective approaches to structure-aided design of vaccines and therapeutics for clinical use [5].

Cryo-EM 3D reconstruction are affected by a loss of contrast at high-resolution because several reasons, including molecular motions, structural heterogeneity, and signal damping by the transfer function of the electron microscope. This high-resolution structural information is essential for the interpretation and understanding of the functional mechanisms of macromolecules. Thus, multiple approaches been proposed in the past to improve the visibility and interpretability of high-resolutions macromolecular details. These methods usually categorized as map postprocessing techniques are based on global and local B-factor sharpening [6–10] or map local sharpening using other sources of information as an estimation of the local map resolution [11], a fitted atomic model [12] or a neural network previously trained with cryo-EM maps and respective sharpened maps using available fitted atomic models [13].

In this work, we propose a novel map enhancing approach to improve the contrast of cryo-EM maps at high-resolution. This method can be used to enhance raw cryo-EM reconstructions before any postprocessing step or, in addition, it can be used after any of the different postprocessing methods presented above. Thus, it can be employed as a post-postprocessing approach if desired. To the best of our knowledge, currently in cryo-EM there is not any map processing approach that could be used as a map post-postprocessing method, accepting as input sharpened and masked maps to further enhance them. In this work, we have focused on this application of the

#444675 https://doi.org/10.1364/OE.444675
Journal © 2022 Received 29 Sep 2021; revised 27 Nov 2021; accepted 17 Dec 2021; published 28 Jan 2022

Optics EXPRESS

approach. The proposed method also provides an estimation of the local resolution map of a cryo-EM reconstruction. Note that previous approaches to estimate the local resolution of a cryo-EM map have been proposed in the past as for example [14,15]. The proposed sharpening and local resolution estimation methods are based on introducing strong structural *a priori* information. The approach determines for the cryo-EM map to be processed the likelihood of showing a tubular (elongated) structure locally, enhancing tubular-like regions while attenuating other geometrical shapes as blob-like or plate-like regions. This structural evaluation is done by analyzing locally the eigenvalues of the Hessian matrix to determine voxel-wise the likelihood that a tubular structure is present. Note that high-resolution macromolecular structures as the backbone and side chains show tube-like (elongated) structures. Thus, the proposed approach aims to enhance these parts while filtering other local structures with other geometries. This filtering process is usually known as Frangi filter and was originally proposed in [16]. Detection of tube-like structures in cryo-EM maps and methods to enhance cryotomograms based on the structure tensor have been proposed in the past before the resolution revolution, as for example [17–19].

2. Proposed method

In the following, we provide a comprehensive description of the proposed approach, which is based on a filtering process to enhance local geometric structures in a cryo-EM map that can be regarded as tubular [16].

We can approximate a cryo-EM map $V(\mathbf{r})$ by its second order Taylor expansion in the vicinity of a point $\mathbf{r}_0$ as

$$V(\mathbf{r}_0 + \Delta\mathbf{r}_0, s) \approx V(\mathbf{r}_0, s) + \Delta\mathbf{r}_0{}^T \cdot \nabla_{\mathbf{r}_0,s} V + \Delta\mathbf{r}_0{}^T \cdot H_{\mathbf{r}_0,s} V \cdot \Delta\mathbf{r}_0 \tag{1}$$

In Eq. (1), $\nabla_{\mathbf{r}_0,s}$ and $H_{\mathbf{r}_0,s}$ are the gradient and Hessian operators computed at $\mathbf{r}_0$ with scale s. Note that the scale refers to the way differentiation is defined. We take derivatives after convolving the map with a Gaussian kernel of size s. Note that because the chain rule, differentiation in this case is equivalent to a convolution with derivatives of Gaussians as

$$\frac{\partial}{\partial x} V(\mathbf{r}, s) = s^{\gamma} V(\mathbf{r}) * \frac{\partial}{\partial x} G(\mathbf{r}, s) \tag{2}$$

with

$$G(\mathbf{r}, s) = 1/(2\pi s^2)^{3/2} \exp(-|\mathbf{r}|^2/2s^2) \tag{3}$$

In Eq. (2), γ is a parameter to control the response of the differential operations at different scales. In our case, as we want to enhance high-resolution details, we use γ=0.5. Note that in Eq. (2), we have defined the Gaussian derivate along x axis only. However, the expressions for the y and z axis are similar. The second derivatives of the Gaussian kernel with size s, shown in Eq. (3), produces a probe kernel that generates maximum response when the map $V(\mathbf{r})$ presents local features with size $2s$ along the derivative direction (please see Fig. 1 in [16]. Thus, the maximum response of Gaussian second order derivatives can be used to determine the size of local map features. In Eq. (1), the Hessian (third element in Eq. (1)) is defined in terms of second order

Optics EXPRESS

derivatives as

$$H_{\mathbf{r}_0,s}V(\mathbf{r},s) = \begin{pmatrix} \partial^2 V(\mathbf{r},s)/\partial x\partial x & \partial^2 V(\mathbf{r},s)/\partial x\partial y & \partial^2 V(\mathbf{r},s)/\partial x\partial z \\ \partial^2 V(\mathbf{r},s)/\partial y\partial x & \partial^2 V(\mathbf{r},s)/\partial y\partial y & \partial^2 V(\mathbf{r},s)/\partial y\partial z \\ \partial^2 V(\mathbf{r},s)/\partial z\partial x & \partial^2 V(\mathbf{r},s)/\partial z\partial y & \partial^2 V(\mathbf{r},s)/\partial z\partial z \end{pmatrix} = \\ = s^{\gamma} V(\mathbf{r}) * \begin{pmatrix} \partial^2 G(\mathbf{r},s)/\partial x\partial x & \partial^2 G(\mathbf{r},s)/\partial x\partial y & \partial^2 G(\mathbf{r},s)/\partial x\partial z \\ \partial^2 G(\mathbf{r},s)/\partial y\partial x & \partial^2 G(\mathbf{r},s)/\partial y\partial y & \partial^2 G(\mathbf{r},s)/\partial y\partial z \\ \partial^2 G(\mathbf{r},s)/\partial z\partial x & \partial^2 G(\mathbf{r},s)/\partial z\partial y & \partial^2 G(\mathbf{r},s)/\partial z\partial z \end{pmatrix} \tag{4}$$

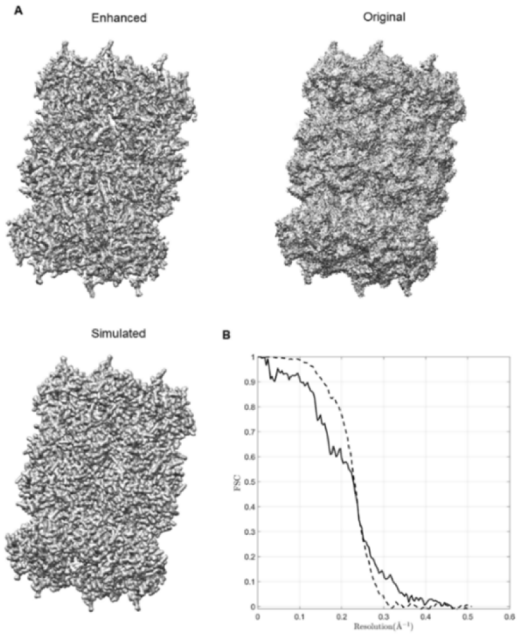

Fig. 1. Results obtained for the simulated T20 proteosome. A) enhanced, original, and simulated maps; B) respective FSCs curves obtained when comparing the enhanced (continuous black curve) and original (dashed black curve) maps with the simulated reconstruction obtained from the atomic structure.

Note that this matrix, is symmetric and square so it can be diagonalized. Eigenvalue analysis of the Hessian matrix provides local principal directions along which the second order map structure can be decomposed. Note that corresponding eigenvalues of the Hessian matrix corresponds to the curvatures of the map at point $\mathbf{r}$ along these principal directions, which include maximal or minimal curvatures. Eigenvalue analysis of the Hessian provides

$$H_{\mathbf{r}_0,s}V(\mathbf{r},s) \cdot \mathbf{u}_{s,k} = \lambda_{s,k} \cdot \mathbf{u}_{s,k} \tag{5}$$

where $\mathbf{u}_{s,k}$ denotes principal direction k obtained when using a Gaussian kernel of size s. Note that the eigenvalues are sorted by magnitude so $|\lambda_{s,1}| \leq |\lambda_{s,2}| \leq |\lambda_{s,3}|$. Equation (5) can be transformed into

$$\mathbf{u}_{s,k}{}^{T} \cdot H_{\mathbf{r}_0,s}V(\mathbf{r},s) \cdot \mathbf{u}_{s,k} = \lambda_{s,k} \tag{6}$$

Thus, the principal direction are three orthogonal directions that are invariant up to a scaling factor when transformed by the Hessian matrix. A comprehensive geometrical interpretation is that a

Optics EXPRESS

sphere of unit radii and centered at $\mathbf{r}_0$ will be transformed by the Hessian matrix into an ellipsoid with axis oriented along the directions given by the eigenvectors and with corresponding semi-axis given by the eigenvalues. This ellipsoid can be used to determine tube-like measures. Note that the principal curvatures of a tube-like structure are characterized by a close to zero (or zero) $|\lambda_{s,1}|$, and large and approximately equal $|\lambda_{s,2}|$ and $|\lambda_{s,3}|$. Moreover, blob-like, and plate-like structures are characterized by $|\lambda_{s,1}| \cong |\lambda_{s,2}| \cong |\lambda_{s,3}|$ and $|\lambda_{s,1}| \cong |\lambda_{s,2}| < |\lambda_{s,3}|$, respectively. Moreover, background voxels usually show small magnitudes for the Gaussian derivatives and eigenvalues, so they are characterized by $|\lambda_{s,1}| \cong |\lambda_{s,2}| \cong |\lambda_{s,3}| \cong 0$. Note in addition, that in cryo-EM 3D reconstructions, macromolecular electron densities appear as bright structures in a darker environment. Thus, eigenvalues must show negative values. Table 1 summarizes typical structural patterns shown in cryo-EM maps according to their eigenvalues.

Table 1. Typical structural patterns depending on the eigenvalue values for cryo-EM maps.

$\lambda_{s,1}$	$\lambda_{s,2}$	$\lambda_{s,3}$	Pattern
Low	Low	High (negative)	Plate-like
Low	High (negative)	High (negative)	Tube-like
High (negative)	High (negative)	High (negative)	Blob-like
Low	Low	Low	Background

According to Table 1, it is possible to determine a tube-like likelihood measure as

$$\chi_s(\mathbf{r}) = \begin{cases} 0 & \text{if } \lambda_2 > 0 \text{ and } \lambda_3 > 0 \\ (1 - \exp(-R_\alpha{}^2/2\alpha^2)) \exp(-R_\beta{}^2/2\beta^2) & (1 - \exp(-R_\kappa{}^2/2\kappa^2)) \end{cases} \tag{7}$$

with

$$\begin{aligned} R_\alpha &= |\lambda_2|/|\lambda_3| \\ R_\beta &= |\lambda_1|/(|\lambda_2\lambda_3|)^{1/2} \\ R_\kappa &= (\lambda_1{}^2 + \lambda_2{}^2 + \lambda_3{}^2)^{1/2} \end{aligned} \tag{8}$$

In Eq. (8), R_α, R_β and R_κ distinguish between background, plate-, blob- and tube-like structures. R_α and R_β show values between 0 and 1. On the other hand, α, β and κ control the sensibility of the filter to R_α, R_β and R_κ. Note, that a tubular local structure is characterized by $R_\alpha \approx 1$, $R_\beta \ll 1$ and $R_\kappa \gg 1$, producing a high value for $\chi_s(\mathbf{r}_0)$, which refers to a local likelihood estimation of tubularness in the cryo-EM map. In all the results shown here, we have used $\alpha = 0.45$, $\beta = 0.45$. A good typical value for κ is half of the mean value of R_κ. However, if a binary solvent mask is provided to the approach, κ is computed from the 90% quantile of the empirical distribution of R_κ, which is generated using voxels values outside the mask only.

The tubularness measure given in Eq. (7) is analyzed for different scales (s) and the value providing the highest value corresponds to the size of the probe kernel that approximately matches the size of the tube-like structure in the cryo-EM map. Thus, the final filter response corresponds to

$$\chi(\mathbf{r}) = \max_{s_{\min} \le s \le s_{\max}} \chi_s(\mathbf{r}) \tag{9}$$

Note that $\chi(\mathbf{r})$ is a map providing values between 0 and 1 and determining the likelihood of finding a local tubular (elongated) structure in the cryo-EM map. Thus, this map can be used as a weighting map to enhance tubular-like regions in map V, while attenuating other geometrical

Optics EXPRESS

shapes as blob-like, plate-like or background regions as

$$\hat{V}(\mathbf{r}) = \chi(\mathbf{r}) \cdot V(\mathbf{r}) \tag{10}$$

where "." refers to voxel wise multiplication. Note that $\chi(\mathbf{r})$ is computed voxel-wise and in real space. Thus, the corresponding density map is weighted locally according to its tube-like likelihood and the defined scale search range given by $s_{\min}$ and $s_{\max}$. This enhancement is done therefore within a defined resolution or scale range, acting thus as a bandpass and tube-pass filter within a typical resolution range of [2–6] Å. Additionally, the scale s that best tune voxel by voxel the cryo-EM map, can be used to obtain a local resolution estimation of map V at the light of the introduced geometrical restrictions.

3. Results

We tested the proposed method with simulated and experimental cryo-EM maps, including recent 3D reconstructions of SARS-CoV-2 related proteins. In all cases, we compared the results obtained by the proposed approach with simulated maps from corresponding atomic models and, in the case of experimental results, with postprocessed maps after B-factor correction [6]. The source code for the presented method is freely available under the terms of an open-source software license and can be downloaded from https://github.com/1aviervargas/frangi.

3.1. T20S proteosome (simulation)

First, we tested the performance of the proposed method with a simulation. To this end, we use the atomic structure of the Thermoplasma Acidophilum 20S proteosome determined at 3.4 Å resolution (PDB ID: 1PMA) to generate a simulated density map of 2.5 Å resolution with Chimera [20]. This simulated 'clean' map is then low-pass filtered by a Gaussian filter of variance 1.5 and corrupted with Gaussian noise resulting in a map with a signal-to-noise ratio (SNR) of 0.4. The SNR is estimated from $SNR = E[V^2]/E[N^2]$, where E refers to the expected value and V and N to the signal and noise terms. This corrupted map is then processed by our proposed enhancement approach. We evaluate the enhanced and corrupted maps by comparing them with the original clean simulated map. We use as evaluation metrics the correlation and the Fourier Shell Correlation (FSC) [6] between maps. The FSC measures the normalized cross-correlation coefficient between two 3D maps over corresponding shells in Fourier space, thus, proving a similarity measure between the maps along different spatial frequencies.

Figure 1A shows the obtained enhanced, clean (simulated), and corrupted (original) maps for the T20 proteosome. As can be seen from this figure, the enhanced map shows much more high-resolution details when compared with the corrupted reconstruction. We also show in Fig. 1(B), the obtained FSCs when comparing the enhanced and corrupted maps with the 'clean' (simulated) reconstruction. As can be seen from the FSC curves, the enhanced map shows lower Fourier correlations at low resolutions, while higher correlations starting from a resolution of 4.1 Å and higher. Thus, the *a priori* information introduced by our proposed approach improves the visibility and interpretability of processed maps at high resolutions, while also acts as a bandpass filter dropping the FSC for low resolution values as explained in the Introduction section. Moreover, the respective correlations between maps are 0.80 and 0.76 when comparing the clean with the enhanced and corrupted maps respectively.

3.2. T20S proteosome

We have also used experimental cryo-EM reconstructions from the Thermoplasma Acidophilum 20S proteosome. Thus, we have used the cryo-EM 3D reconstruction deposited in the Electron Microscopy Data Bank (EMDB) [21] with ID EMD-6287 after postprocessing by B-factor sharpening. This map, which reports a Gold-standard FSC resolution of 2.8 Å, is enhanced by

Optics EXPRESS

the proposed approach and then compared with the simulated map computed from the fitted atomic structure (PDB ID: 1PMA). As before, we use as evaluation metrics the correlation and the Fourier Shell Correlation (FSC) between maps.

In Fig. 2(A), we show the enhanced, original, and simulated maps. Additionally, in Fig. 2(B), we show respective zoomed views of the respective red rectangles shown in Fig. 2(A). As can be seen from these figures, the enhanced map shows improved high-resolution details when compared with the original reconstruction. We have also computed respective FSCs curves obtained when comparing the enhanced (continuous black curve) and original (dashed black curve) maps with the simulated reconstruction obtained from the atomic structure. These FSCs are shown in Fig. 2(C). As can be seen from Fig. 2(C), starting from a resolution of 2.7 A, the enhanced reconstruction provides higher FSCs showing improved similarity with the simulated map. Note additionally that all FSC values are above zero for all resolution values inside the used interval. Moreover, to analyze if the improvement in the FSC shown in Fig. 2(A) could be explained by a masking operation, we low-pass filtered the obtained $\chi(\mathbf{r})$ map with a Gaussian filter of variance 1.0 before multiplying it to the original cryo-EM map. The corresponding FSC between this enhanced-filtered map and the simulated reconstruction is shown in Fig. 2(A) in a dashed curve with dots. Note that this curve is also above the FSC of the original map, so the improvement obtained is because the *a priori* information introduced by our enhancing approach. Corresponding correlations between the enhanced and original maps with the simulated reconstruction are 0.87 and 0.88 respectively. Finally, in Fig. 2(D), we show the enhanced 3D reconstruction rendered with different colors indicating the scale of the Gaussian kernel producing the best tuning with the local structure of the map, thus, producing an estimation of the local resolution of the map at the light of the introduced geometrical priors.

3.3. SARS-CoV-2 RBD-62 in complex with ACE2 peptidase domain

We have also enhanced cryo-EM reconstructions of SARS-CoV-2 related proteins. First, we processed the cryo-EM 3D reconstruction of the SARS-CoV-2 receptor binding domain (RBD) in complex with the angiotensin-converting enzyme 2 (ACE2) peptidase domain [22], which is deposited and publicly available in EMDB (EMDB-ID: EMD-12187). This reconstruction corresponds to a 2.9 Å cryo-EM map of the high-affinity complex of RBD-62 and ACE2, including all rapidly spreading mutations that provides a structural bases for future drug and vaccine development and for in silico evaluation of known antibodies [22].

As before, we compared the original (deposited) B-factor sharpened reconstruction and the obtained enhanced map by our proposed approach, with the simulated map computed from the corresponding atomic model (PDB ID: 7BH9). In Fig. 3(A), we show the different maps at a low-density level. As can be seen from Fig. 3(A), the simulated map does not cover the whole complex. Thus, for comparison purposes, we extracted the region covered by the simulated map in the enhanced and original maps using the same extended and soft mask. These masked maps can be seen in Fig. 3(B), where the enhanced map shows higher resolution details that the original reconstruction. As before, we computed respective FSCs curves comparing the enhanced (continuous black curve) and original (dashed black curve) maps with the simulated reconstruction obtained from the atomic structure. We used masked maps for these comparisons. These FSCs are shown in Fig. 3(C). As can be seen from this figure, starting from a resolution of 2.7 Å, the enhanced reconstruction provides higher FSCs showing improved similarity with the simulated map. Moreover, the correlations between the enhanced and original maps with the simulated reconstruction are 0.85 and 0.86 respectively In Fig. 3(D), we show the estimated local resolutions in Angstroms (Å) of the original map, rendered with different colors at the light of the geometric priors introduced by our proposed approach.

Optics EXPRESS

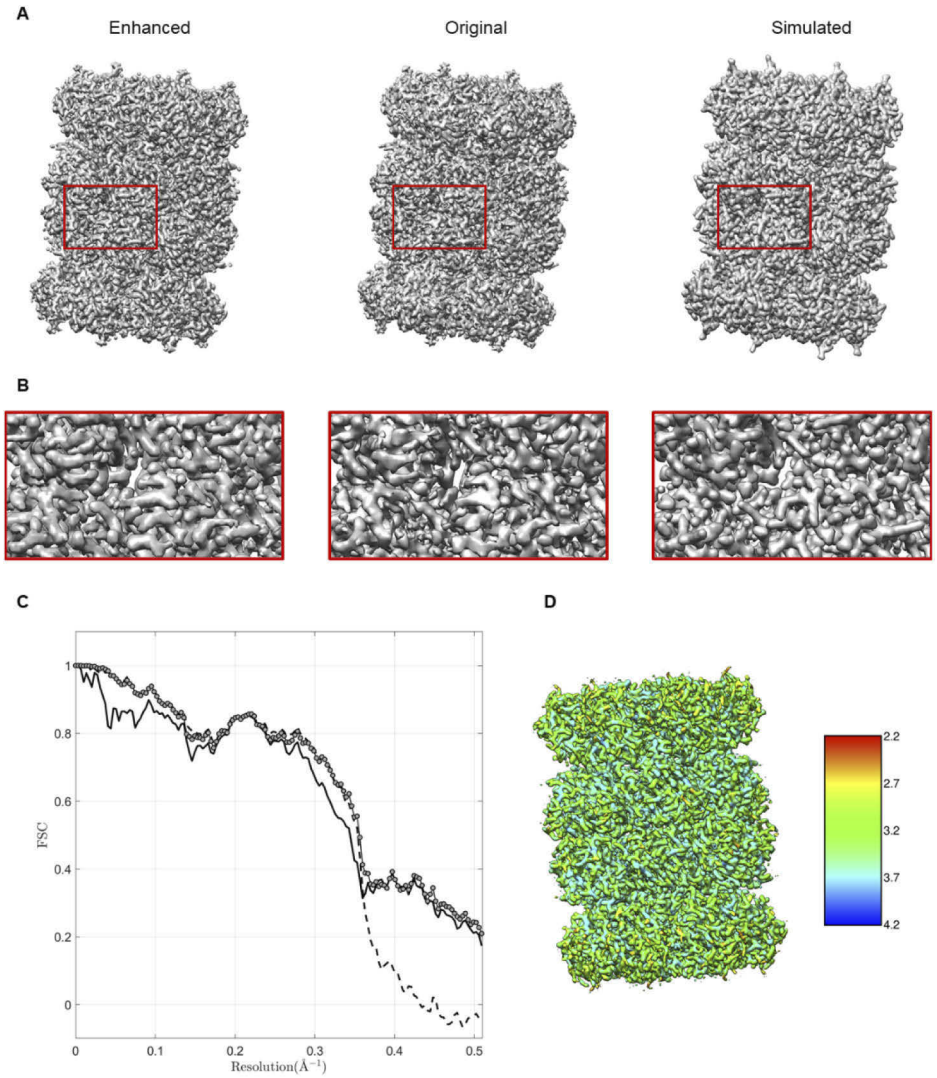

Fig. 2. Results obtained for the T20 proteosome. A) enhanced, original, and simulated maps; B) corresponding zoomed views of the red squares shown above; C) respective FSCs curves obtained when comparing the enhanced (continuous black curve), original (dashed black curve) and enhanced filtered (continuous black curve with dots) maps with the simulated reconstruction obtained from the atomic structure; D) estimated local resolution map computed from the scale of the Gaussian kernel producing the best tuning with the local structure in Angstroms (Å).

3.4. SARS-CoV-2 spike protein in complex with neutralizing antibody

Secondly, we processed a recent cryo-EM reconstruction of neutralizing antibody 5-7 in complex with the SARS-CoV-2 spike protein [23]. This cryo-EM reconstruction is deposited and publicly available in EMDB (EMDB-ID: EMD-24708) and reports a FSC global resolution of 3.7 Å. This reconstruction shows a potent NTD-directed neutralizing antibody 5-7, which recognizes a site distinct from other potently neutralizing antibodies.

Optics EXPRESS

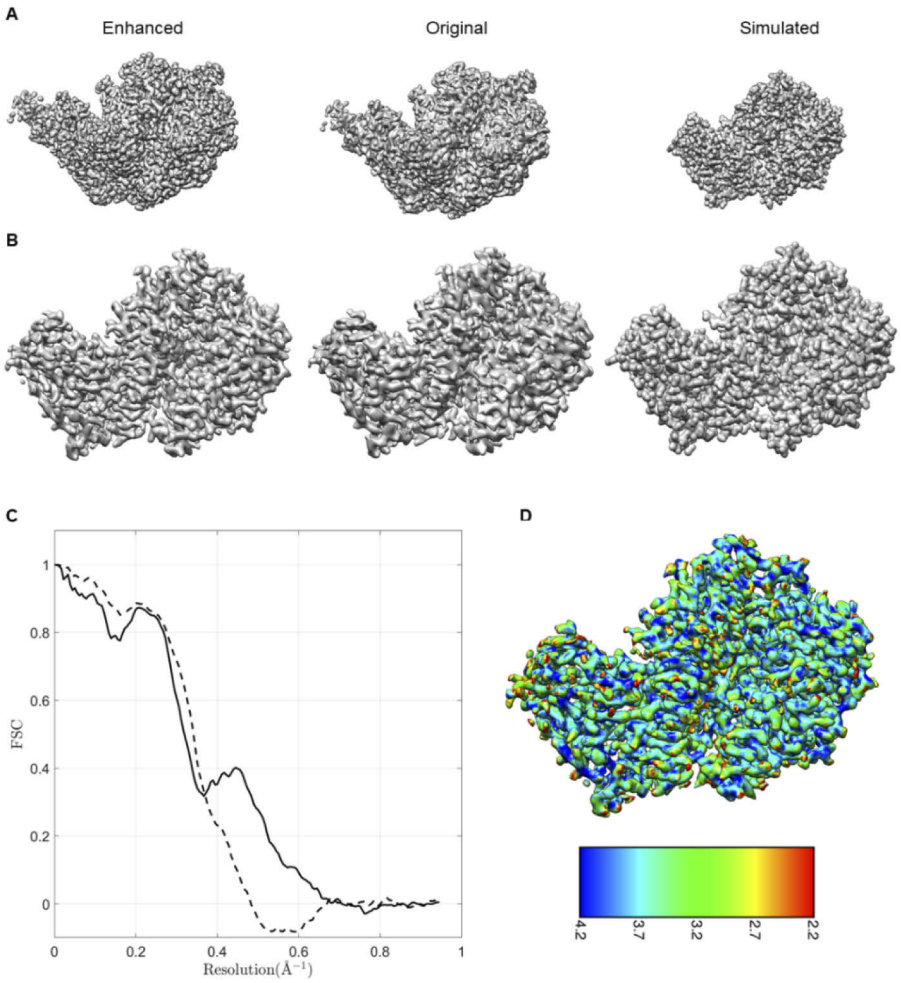

Fig. 3. Results obtained for the SARS-CoV-2 RBD-62 in complex with ACE2 peptidase domain. A) enhanced, original, and simulated maps; B)) masked enhanced, original, and simulated maps to the volume occupied by the simulated map; C) respective FSCs curves obtained when comparing the enhanced (continuous black curve) and original (dashed black curve) maps with the simulated reconstruction obtained from the atomic structure; D) estimated local resolution map computed from the scale of the Gaussian kernel producing the best tuning with the local structure in Angstroms (Å).

This postprocessed map (EMD-24708) is enhanced by the proposed approach and then compared with the simulated map computed from the fitted atomic structure (PDB ID: 7RW2). As before, we use as evaluation metrics the Fourier Shell Correlation (FSC) between maps. In Fig. 4(A), we show the enhanced, original, and simulated maps. From this figure, at the used density level, the original map does not show high-resolution features and seems to be stretched because the presence of preference sample orientations. Oppositely, the obtained enhanced map shows high-resolution details and seems not to be stretched. Moreover, the simulated map does not cover the whole complex. Thus, for comparison purposes, we extracted the region covered by the simulated map in the enhanced and original maps using the same extended and soft mask. These masked maps are shown in Fig. 4(B). In Fig. 4(C), we show zoomed views of the maps to appreciate high-resolution details. Figure 4(D) shows FSCs curves comparing

Optics EXPRESS

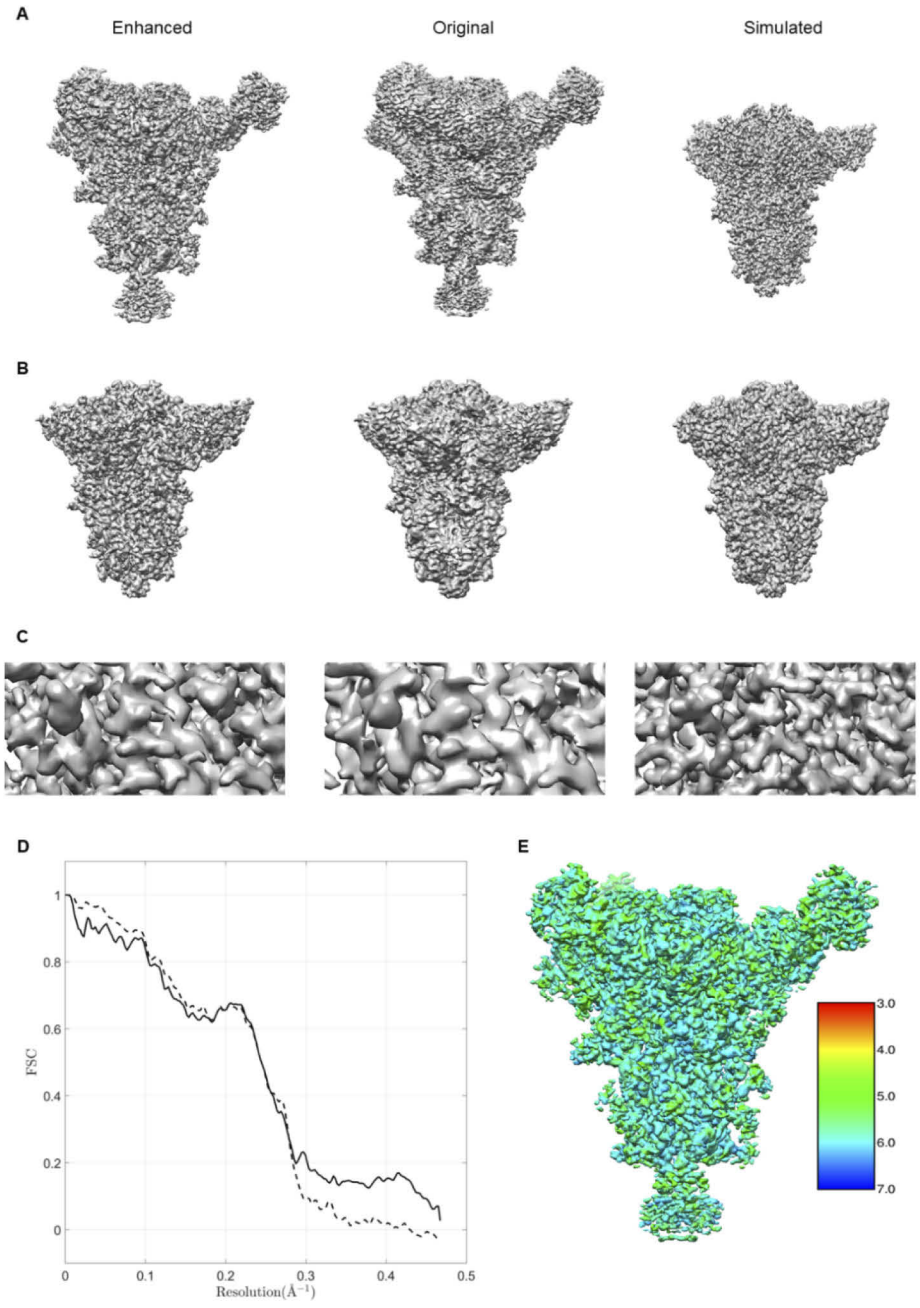

Fig. 4. Results obtained for the SARS-CoV-2 spike protein in complex with the neutralizing antibody 5-7 in complex. A) enhanced, original, and simulated maps; B) masked enhanced, original, and simulated maps to the volume occupied by the simulated map; C) corresponding zoomed views of the enhanced, original, and simulated maps; D) respective FSCs curves obtained when comparing the enhanced (continuous black curve) and original (dashed black curve) maps with the simulated reconstruction obtained from the atomic structure; D) estimated local resolution map computed from the scale of the Gaussian kernel producing the best tuning with the local structure in Angstroms (Å).

Optics EXPRESS

masked enhanced (continuous black curve) and original (dashed black curve) maps with the simulated reconstruction obtained from the atomic structure. As before, these curves show that our enhanced map is more similar to the simulated reconstruction at high resolutions thanks to the *a priori* structural information introduced. Finally, Fig. 4(E) shows the enhanced map colored with estimated local resolutions in Angstroms (Å) of the original map.

Moreover, in Fig. 5, we compare obtained local resolution maps by our proposed method with the resolution maps computed by MonoRes approach [14].

As can be seen from Fig. 5, the proposed approach produces local resolution maps showing similar but lower values than MonoRes. A possible reason of these differences is that the proposed approach introduces additional geometrical constrains, as the tube-like likelihood, to determine the size of the local structure. Finally, in Fig. 6, we analyze the performance of the method in relation to the noise presented in the map. To this end, we corrupt the simulated reconstruction of the T20S proteosome with different levels of noise to produce maps with SNRs of 0.9, 0.4, 0.2, 0.15 and 0.1. In each case, we enhance these noisy maps with our proposed approach and calculate the FSCs between the corrupted (noisy) and the clean simulated (noise-free) maps, and between the enhanced and the clean simulated maps. As can be seen from Fig. 6, in all these cases the proposed method boosts the FSC at high resolutions.

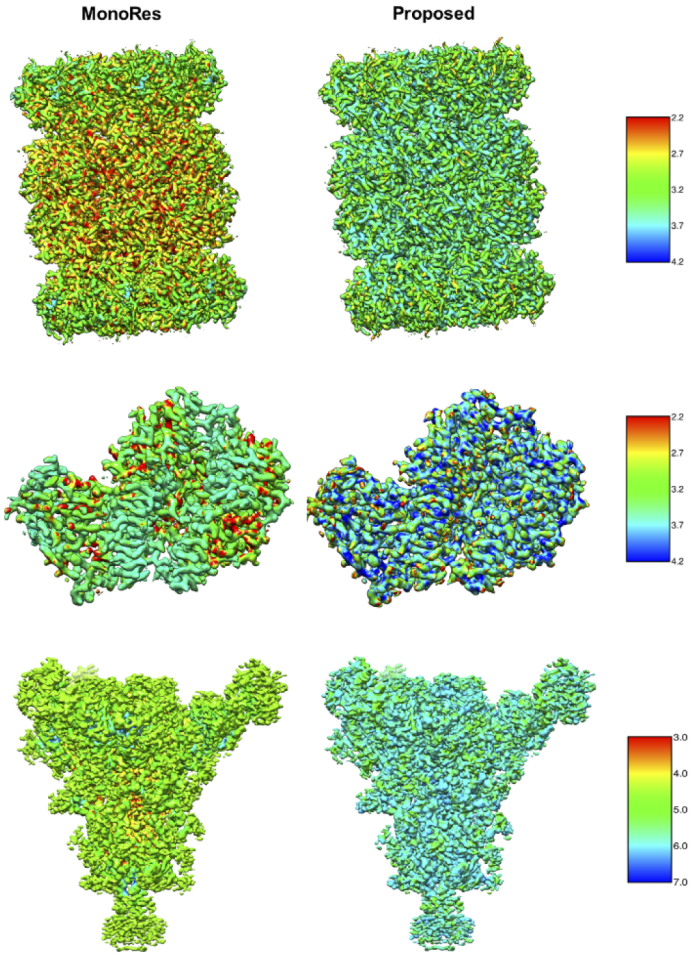

Fig. 5. Obtained local resolution maps computed by MonoRes and the proposed approach.

Optics EXPRESS

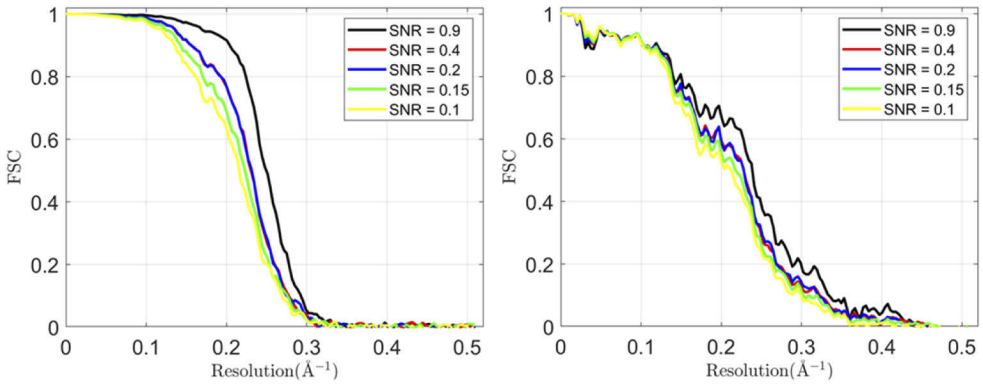

Fig. 6. Left: FSCs curves obtained comparing simulated noisy maps showing different SNRs, with the simulated reconstruction (noise-free). Right: FSCs curves obtained when comparing the enhanced maps with the simulated reconstruction (noise-free).

4. Conclusions

In this work, we introduce a method to enhance cryo-electron microscopy maps (cryo-EM). The proposed method can be used with cryo-EM maps before and/or after any postprocessing step. Thus, it can be used as an additional enhancement tool after map sharpening. In this work, we have focused on this application, thus, the experimental maps used in the Results section were previously postprocessed. To the best of our knowledge, currently in cryo-EM there is not any map processing approach that could be used as a map post-processing method.

The approach is based on a multiscale tubular filter that determines the likelihood of finding tube-like structures locally within a defined scale range. Then, tube-like regions are enhanced, while background, plate-like and blob-like zones are attenuated. The method introduces *a priori* information in the 3D reconstructions making use of the fact that typical macromolecular structures as the backbone or side chains show tubular (elongated) shapes for maps at resolutions between approximately [2–6] Å. Thus, the proposed approach aims to enhance these elongated structures while, filtering other local structures with other geometries. This enhancement is done therefore within a defined resolution or size range acting thus as a bandpass and tube-pass filter for a typical resolution between [2–6] Å. For maps within this resolution range, we recommend using the input parameters shown in Section 2. Note that for maps with resolutions not included in the range [2–6] Å, the proposed method should be used with caution and likely with different input parameters. For example, in case of processing maps showing atomic resolution, it should be better to enhance blob-like structures rather than tube-like regions.

The proposed approach can also estimate the local resolution of the processed cryo-EM map at the light of the introduced geometrical priors. The method finds the maximum combined response of descriptors R_α, R_β and R_κ along a given scale range and determines the size at which the Gaussian derivatives are best tuned with the local structure considering also the similarity of the local structure with a tube-like structure. The estimation of local resolution maps from our proposed approach is limited to resolution ranges between [2–6] Å, where local map structures show tube-like (elongated) structures. Note that for maps with resolutions not included in the range [2–6] Å, the proposed method should be used with caution. Moreover, we have compared local resolution maps obtained by our proposed method and by MonoRes approach [14]. Our approach produces resolution maps showing similar but lower values than MonoRes. A possible explanation of these discrepancies is that the proposed approach considers additional constrains, as the tube-like likelihood, to determine the size of local structures.

Optics EXPRESS

We tested the proposed method with different macromolecules, including recent reconstructions of the SARS-CoV-2 (EMD-12187 and EMD-24708). Our results show that our method can improve obtained postprocessed reconstructions, producing maps that are more similar that simulated maps from atomic models at high-resolutions. Thus, the approach can be used to improve the interpretability and analysis of cryo-EM maps at high-resolution. The source code of the used methods is publicly available from https://github.com/1aviervargas/frangi so all the results shown here can be reproduced independently.

Funding. Ministerio de Ciencia e Innovación (PID2019-108850RA-I00).

Disclosures. The authors declare no conflicts of interest.

Data availability. Data underlying the results presented in this paper are available in Ref. [21]

References

1. K. M. Yip, N. Fischer, E. Paknia, A. Chari, and H. Stark, "Atomic-resolution protein structure determination by cryo-EM," Nature **587**(7832), 157–161 (2020).
2. T. Nakane, A. Kotecha, A. Sente, G. McMullan, S. Masiulis, P. Brown, I. T. Grigoras, L. Malinauskaite, T. Malinauskas, J. Miehling, T. Uchanski, L. Yu, D. Karia, E. V. Pechnikova, E. de Jong, J. Keizer, M. Bischoff, J. McCormack, P. Tiemeijer, S. W. Hardwick, D. Y. Chirgadze, G. Murshudov, A. R. Aricescu, and S. H. W. Scheres, "Single-particle cryo-EM at atomic resolution," Nature **587**(7832), 152–156 (2020).
3. D. Wrapp, N. Wang, K. S. Corbett, J. A. Goldsmith, C. L. Hsieh, O. Abiona, B. S. Graham, and J. S. McLellan, "Cryo-EM structure of the 2019-nCoV spike in the prefusion conformation," Science **367**(6483), 1260–1263 (2020).
4. A. C. Walls, Y. J. Park, M. A. Tortorici, A. Wall, A. T. McGuire, and D. Veesler, "Structure, Function, and Antigenicity of the SARS-CoV-2 Spike Glycoprotein," Cell **181**(2), 281–292.e6 (2020).
5. H. Yang and Z. Rao, "Structural biology of SARS-CoV-2 and implications for therapeutic development," Nat Rev Microbiol **19**(11), 685–700 (2021).
6. P. B. Rosenthal and R. Henderson, "Optimal determination of particle orientation, absolute hand, and contrast loss in single-particle electron cryomicroscopy," J. Mol. Biol. **333**(4), 721–745 (2003).
7. J. J. Fernandez, D. Luque, J. R. Caston, and J. L. Carrascosa, "Sharpening high resolution information in single particle electron cryomicroscopy," J. Struct. Biol. **164**(1), 170–175 (2008).
8. S. H. Scheres, "Semi-automated selection of cryo-EM particles in RELION-1.3," J. Struct. Biol. **189**(2), 114–122 (2015).
9. T. C. Terwilliger, O. V. Sobolev, P. V. Afonine, and P. D. Adams, "Automated map sharpening by maximization of detail and connectivity," Acta Crystallogr D Struct. Biol. **74**(6), 545–559 (2018).
10. S. Kaur, J. Gomez-Blanco, A. A. Z. Khalifa, S. Adinarayanan, R. Sanchez-Garcia, D. Wrapp, J. S. McLellan, K. H. Bui, and J. Vargas, "Local computational methods to improve the interpretability and analysis of cryo-EM maps," Nat. Commun. **12**(1), 1240 (2021).
11. J. L. V. Erney Ramirez-Aportela, J. L. Vilas, A. Glukhova, R. Melero, P. Conesa, M. Martinez, D. Maluenda, J. Mota, A. Jimenez, J. Vargas, R. Marabini, P. M. Sexton, J. M. Carazo, and C. O. S. Sorzano, "Automatic local resolution-based sharpening of cryo-EM maps," Bioinformatics **36**, 765–772 (2020).
12. A. J. Jakobi, M. Wilmanns, and C. Sachse, "Model-based local density sharpening of cryo-EM maps," eLife **6**, e27131 (2017).
13. R. Sanchez-Garcia, J. Gomez-Blanco, A. Cuervo, J. M. Carazo, C. O. S. Sorzano, and J. Vargas, "DeepEMhancer: a deep learning solution for cryo-EM volume post-processing," Commun. Biol. **4**(1), 874 (2021).
14. J. L. Vilas, J. Gomez-Blanco, P. Conesa, R. Melero, J. Miguel de la Rosa-Trevin, J. Oton, J. Cuenca, R. Marabini, J. M. Carazo, J. Vargas, and C. O. S. Sorzano, "MonoRes: Automatic and Accurate Estimation of Local Resolution for Electron Microscopy Maps," Structure **26**(2), e334 (2018).
15. A. Kucukelbir, F. J. Sigworth, and H. D. Tagare, "Quantifying the local resolution of cryo-EM density maps," Nat. Methods **11**(1), 63–65 (2014).
16. R. Frangi, W. J. Niessen, K. Vincken, and M. Viergever, "Multiscale Vessel Enhancement Filtering," Med. Image Comput. Comput. Assist. Interv. **1496**, 130–137 (2000).
17. Z. Yu and C. Bajaj, "Computational approaches for automatic structural analysis of large biomolecular complexes," IEEE/ACM Trans. Comput. Biol. and Bioinf. **5**(4), 568–582 (2008).
18. Z. Yu and C. Bajaj, "A Structure Tensor Approach for 3D Image Skeletonization: Applications in Protein Secondary Structure Analysis," in *2006 International Conference on Image Processing*, (2006), pp. 2513–2516.
19. J. J. Fernandez and S. Li, "An improved algorithm for anisotropic nonlinear diffusion for denoising cryo-tomograms," J. Struct. Biol. **144**(1-2), 152–161 (2003).
20. E. F. Pettersen, T. D. Goddard, C. C. Huang, G. S. Couch, D. M. Greenblatt, E. C. Meng, and T. E. Ferrin, "UCSF Chimera–a visualization system for exploratory research and analysis," J. Comput. Chem. **25**(13), 1605–1612 (2004).
21. C. L. Lawson, M. L. Baker, C. Best, C. Bi, M. Dougherty, P. Feng, G. van Ginkel, B. Devkota, I. Lagerstedt, S. J. Ludtke, R. H. Newman, T. J. Oldfield, I. Rees, G. Sahni, R. Sala, S. Velankar, J. Warren, J. D. Westbrook, K. Henrick,

Optics EXPRESS

G. J. Kleywegt, H. M. Berman, and W. Chiu, "EMDataBank.org: unified data resource for CryoEM," Nucleic Acids Res. **39**(Database), D456–464 (2011).

22. J. Zahradnik, S. Marciano, M. Shemesh, E. Zoler, D. Harari, J. Chiaravalli, B. Meyer, Y. Rudich, C. Li, I. Marton, O. Dym, N. Elad, M. G. Lewis, H. Andersen, M. Gagne, R. A. Seder, D. C. Douek, and G. Schreiber, "SARS-CoV-2 variant prediction and antiviral drug design are enabled by RBD in vitro evolution," Nat. Microbiol. **6**(9), 1188–1198 (2021).
23. G. Cerutti, Y. Guo, P. Wang, M. S. Nair, Y. Huang, J. Yu, L. Liu, P. S. Katsamba, F. Bahna, E. R. Reddem, P. D. Kwong, D. D. Ho, Z. Sheng, and L. Shapiro, "Neutralizing antibody 5-7 defines a distinct site of vulnerability in SARS-CoV-2 spike N-terminal domain," bioRxiv 10.1101/2021.06.29.450397 (2021).